Published in final edited form as:
Phys Med Biol. 2013 June 21; 58(12): . doi:10.1088/0031-9155/58/12/4031.

TOF PET offset calibration from clinical data

M E Werner[1] and **J S Karp**[1,2]

M E Werner: matt.werner@uphs.upenn.edu

[1]Department of Radiology, The University of Pennsylvania, Philadelphia, PA 19104, USA

[2]Department of Physics and Astronomy, The University of Pennsylvania, Philadelphia, PA 19104, USA

Abstract

In this paper, we present a timing calibration technique for time-of-flight positron emission tomography (TOF PET) that eliminates the need for a specialized data acquisition. By eliminating the acquisition, the process becomes fully automated, and can be performed with any clinical data set and whenever computing resources are available. It also can be applied retroactively to datasets for which a TOF offset calibration is missing or suboptimal. Since the method can use an arbitrary data set to perform a calibration prior to a TOF reconstruction, possibly of the same data set, one also can view this as reconstruction from uncalibrated data. We present a performance comparison with existing calibration techniques.

1. Introduction

PET imaging involves the near-simultaneous detection of photons pairs emitted from positron annihilation events within a spatial distribution of radioactivity. Since each annihilation event is known to emit two 511 keV photons in opposite directions, if we assume no further interactions, we can infer that the point of emission is along a line-of-response (LOR) between the two points of detection with uniform probability. If, in addition, the scanner is capable of recording the relative detection times of the two photons, we can estimate the location of the point along the LOR and use this information to improve the speed and quality of image reconstruction. This is known as TOF PET imaging. The application of TOF PET in clinical studies, particularly oncology, has been shown to improve lesion detection (Kadrmas *et al* 2009, Surti *et al* 2011, El Fakhri *et al* 2011) as well as the accuracy and precision of lesion uptake measurements (Surti *et al* 2007, Karp *et al* 2008, Lois *et al* 2010.)

The detection process for TOF PET is illustrated in figure 1, where a photon pair emitted from point E is detected at points A and B.

If the true photon arrival times at A and B are t_A and t_B, then the distance of the emission point along the LOR starting at point A can be calculated using (1).

$$d=\frac{L}{2}+\frac{c}{2}(t_A-t_B) \quad (1)$$

Here, L is the modeled distance between points A and B, and c is the speed of light. Since only time *differences* are considered, we can reference the photon arrival times to the time of emission. With this choice, the variables t_A and t_B represent the TOF of the photons, and will be referred to as such below.

In practice, the measured TOF difference will be subject to noise. The resulting distribution of measurements along an LOR is well modeled by a Gaussian, as depicted in figure 1. The width of this distribution, often referred to as the TOF resolution, imposes an intrinsic limit on the benefit of TOF information. The distribution's full-width-at-half-maximum (FWHM) is often quoted among the performance metrics of TOF PET scanners. For example, the first commercial TOF PET/CT scanner, the LYSO-based Philips Healthcare Gemini TF, which is in clinical operation at the University of Pennsylvania, exhibits a mean TOF resolution of 650 ps (9.8 cm) FWHM. Newer scanners from Philips, Siemens and GE have TOF resolutions in the range of 500–600 ps FWHM. In our lab, we have developed a prototype $LaBr_3$-based TOF PET scanner with a TOF resolution of 375 ps (5.6 cm) FWHM (Karp *et al* 2005, Daube-Witherspoon *et al* 2010.)

In addition to noise, the measured photon detection times, t'_A and t'_B, may be subject to biases δ_A and δ_B. If the biases are unequal, the modeled distance to the distribution mean, d', will be displaced along the LOR from its true location according to (2).

$$d' = \frac{L}{2} + \frac{c}{2}(t'_A - t'_B) = d + \frac{c}{2}(\delta_A - \delta_B) \quad (2)$$

The cumulative effect from TOF biases in all LORs passing through E is an increased spread in the uncertainty. Left uncorrected, this leads to an effective loss of TOF resolution and reduced benefit of TOF to image quality. Maximizing the potential of TOF PET requires a calibration for the timing information in addition to the usual calibrations for detector efficiency, energy and spatial linearity. Originally studied in the 1980s, TOF calibration and reconstruction techniques were re-introduced in commercial PET/CT scanners first by Philips (Surti *et al* 2007,) followed by Siemens (Jakoby *et al* 2011) and GE (Bettinardi *et al* 2011.)

Differences in TOF bias between crystals may be due to differences in crystal scintillation behavior, pulse discrimination, signal amplification, optical pathway length, and electronic delay. Some sources of bias are relatively static, and can be mitigated at the time of manufacture or installation. Other sources drift over the course of days or weeks due to fluctuations in the scanner environment, component degradation, and interactions with other calibrations. Therefore, scanners require periodic re-calibration. It is not necessary to achieve perfect hardware timing synchronization, but rather to estimate the TOF bias for each crystal. We then apply an additive correction to the TOF data in each list event during reconstruction. The correction is referred to as a TOF offset, and it is equal to the negative of the expected TOF bias. We refer to the process of generating these offsets as TOF offset calibration.

An image of the TOF offsets generated by Philips software for the first 10 of the 28 modules of our Gemini TF is shown in figure 2(a). Each pixel represents a single crystal in the scanner. The crystals are shown "unwrapped" from the circumference of the scanner. Note that the location of the crystals relative to nearby PMTs is related to the optical pathway length, which is one contributor to TOF bias. The locations of the PMTs are apparent in the image, as are discontinuities caused by the module-based architecture of the detector despite the fact that modules share columns of PMTs at their boundaries. Note that these data already include a correction for module timing alignment, a calibration procedure commonly performed on PET scanners in order to minimize the coincidence detection window (e.g. Lenox *et al* 2002.)

A variety of methods have been proposed for the timing calibration of TOF PET scanners, including the use of separate reference detectors temporarily placed in coincidence with the

PET scanner for the duration of the TOF offset calibration procedure (Thompson *et at* 2005.) Others have proposed scanning a centered cylindrical phantom, and using an iterative correction to estimate the TOF offsets required to center the resulting TOF histograms for each crystal (Lenox *et al* 2006, Casey *et al* 2012.) In many ways, the algorithm we propose in this paper is a generalization of the latter approach.

At the University of Pennsylvania, we've used two methods for TOF offset calibration that avoid the need for additional detectors, but which still require a specialized data acquisition. The first calibration method is possible with dedicated PET scanners that are equipped with an annular rotating ring used to hold a ^{137}Cs point source during a transmission scan. During TOF offset calibration, we instead fit the ring with an axially aligned liquid line source filled with ^{18}F, which rotates at a radius that is larger than the transverse field-of-view (FOV) (Perkins *et al* 2005.) By collecting data for at least one full rotation, we can observe events for all detectable LORs intersecting the transverse FOV, as shown in figure 3.

Each list event includes indices identifying detecting crystals A and B, and an integer representing the measured TOF difference, $t'_A - t'_B$, in units of 25 ps. From timestamp data embedded within the list, we calculate the true location of the line source, and hence the true TOF difference, $t_A - t_B$, for the event to 25 ps precision. We then calculate the TOF error for crystal A as $error_A = (t'_A - t'_B) - (t_A - t_B)$. We use this to increment a bin in a TOF error histogram for crystal A, and its negative to increment a similar histogram for crystal B, since $error_B = -error_A$. An example of the histogram accumulated for a single crystal is shown in figure 4. Note that all histograms use the same 25 ps bin size as the data itself.

If the mean of a crystal's TOF error histogram is non-zero, the difference is due to a TOF bias specific to the crystal, along with a combination of TOF biases due to all coincident crystals as shown in (3).

$$\overline{error}_A = \frac{1}{N}\sum_i [(t'^i_A - t'^i_{B_i}) - (t^i_A - t^i_{B_i})] = \frac{1}{N}\sum_i \left(t'^i_A - t^i_A\right) - \frac{1}{N}\sum_i \left(t^i_{B_i} - t'^i_{B_i}\right) \quad (3)$$

Here, N is the total number of events with crystal A as an endpoint, and i is an index over those events. The first sum is the mean of the TOF error histogram. This is then split into two sums representing the TOF errors due to the average TOF bias in crystal A and the average TOF bias of all coincident crystals. Since each event is binned twice, with opposite signs for TOF error, the average TOF bias for all crystals in the scanner is zero. As we will discuss later, an assumption made in our work is that the average TOF bias of any large contiguous group of crystals is zero. It follows that we assume the last sum in (3) is zero. Therefore, we compute the TOF offset correction for a crystal as the negative of the average of that crystal's TOF error histogram. Like the TOF difference, the TOF offset for each crystal is stored as an integer representing units of 25 ps.

The second calibration method is used for PET/CT scanners, such as the Philips Healthcare Gemini TF and Gemini TF Big Bore. These scanners employ CT-based attenuation correction, and therefore lack a rotating ring. Instead, we use a centered ^{22}Na point source mounted within a 7 cm O.D. steel scattering cylinder (Perkins *et al* 2005, Griesmer *et al* 2008). Using a low energy gate to detect photons scattered through large angles, we're able to acquire events for all LORs intersecting the transverse FOV as shown in figure 5.

One can use the energies of the detected photons to determine the more likely scattering point. Combining this with the known location of the point source, we are able to histogram the TOF error and determine TOF offsets from (3), as before. Data acquisition is simpler for this method, but the result is arguably less precise.

The methods described above rely on comparing observed TOF distributions with the easily predicted TOF distributions of a simple emission source, scanned especially for that purpose. In the next section, we present an algorithm that generalizes this approach to use data from arbitrary emission distributions.

2. Methods

Our algorithm applies ray-tracing techniques to generate the expected TOF distributions for an arbitrary emission distribution. In particular, we propose using the patient (or phantom) studies generated by normal scanner operations. We assume as inputs a fully corrected reconstructed image of the object, the list data including prompt and delay events, corresponding sinograms for attenuation and efficiency correction, and a TOF scatter estimate. We discuss these in more detail below. The algorithm can be divided into three main steps.

The first step is to accumulate the TOF data from the list used to generate the image into a set of TOF histograms corresponding to each crystal in the scanner. For each prompt event in the list, we consider the recorded TOF difference, $t'_A - t'_B$. We apply any *a priori* TOF offset correction that is available, and increment the corrected $t'_A - t'_B$ bin in the histogram for crystal A, and the $t'_B - t'_A$ bin in the histogram for crystal B, using a weight provided by the efficiency correction sinogram. Delay events are handled similarly, except that we subtract from the histograms. However, since the probability distribution of TOF differences for random (and hence delay) events is known to be uniform, we reduce noise by instead subtracting 1/N from *all* TOF bins in both histograms, where N is the number of possible TOF values that can appear in the list event. This resulting set of histograms will exhibit any uncorrected TOF biases present in the data.

The second step is to generate a set of unbiased model histograms corresponding to each crystal. We start by generating $t_A - t_B$ histograms for true events by ray tracing a reconstructed image. Fully corrected images of sufficient quality can be obtained using non-TOF reconstruction or TOF reconstruction with suboptimal TOF offset calibration. For each measurable LOR, we trace a path through the image to obtain an ideal estimate of the trues TOF profile as shown in figure 6(a) and 6(b).

Next, we convolve each profile with a Gaussian kernel representing the estimated TOF resolution, and scale it using the corresponding entry from the attenuation sinogram. The result is depicted in figure 6(c). The convolved TOF profile is added to the model TOF histogram corresponding to crystal A, and again to the histogram corresponding to crystal B, but with the TOF sense negated.

Finally, we complete our model TOF histograms using $t_A - t_B$ histograms for scattered events generated by an external TOF single scatter simulation (Werner *et al* 2006). The scatter histograms are scaled to fit the list data by the scatter simulation, but the trues histograms from above are not yet scaled properly. Therefore, before adding the scatter to the trues to form the model histograms, we scale the trues so that the sum of each list data histogram is equal to the sum of the corresponding scaled trues plus scatter histograms. The result is a set of unbiased model histograms for each crystal. Examples of the list and model histograms for a single crystal are shown in figure 7. A significant TOF bias is apparent.

The third and final step is to compare, for each crystal, the two corresponding data and model TOF histograms and estimate the TOF offset that will bring them into alignment. We choose the TOF offset which maximizes the cross-correlation between the modeled and measured histograms according to (4).

$$offset_A = argmax_d \int_{-W}^{+W} hist_A^{model}(s) \cdot hist_A^{list}(s+d)\, ds \quad (4)$$

Here, $[-W,+W]$ is the window over which the correlations are computed, and d represents possible TOF offsets. We have used $W \approx 2$ ns in our studies.

To reduce the uncertainty of the TOF offset estimate, one can combine the data from any number of data sets to reduce the noise in the histograms of the TOF list data. For example, our whole-body scans are acquired as a sequence of "frames", corresponding to discrete bed positions. The overlapping frames are processed independently and the images blended to form the final whole body image. We have studied the performance of our algorithm both on a single frame of data as well as on the combined data from multiple frames of a whole-body patient study. One could even maintain a sliding sum of frame histograms from multiple studies. In practice, we further improve accuracy by considering only LORs that pass through the object, because the trues TOF profile is far more peaked than the scatter TOF profile. This makes the cross-correlation maximum even more well-defined.

Since the algorithm can benefit from *a priori* TOF offset correction data, we've implemented it as an iterative algorithm. After each pass through the list, having applied any *a priori* TOF offset correction, we have an estimate of the additional TOF correction needed for each crystal. Using relaxation, we can apply some or all of this correction as shown in (5), and conditionally take another pass through the list data.

$$offset_A^i = offset_A^{i-1} + k \cdot offset_A \quad (5)$$

Here, $offset^{i-1}_A$ is the estimate of the TOF offset prior to iteration i, k is the relaxation factor, $offset_A$ is the estimate of the additional offset required from (4), and $offset^i_A$ is the updated TOF offset. We have used $k=0.6$ in our studies.

Note that the resulting TOF offset table is not unique in the sense that a constant added to all offsets will not be observable or detrimental to reconstruction since only TOF *differences* are considered. However, to make the solution well determined, we arbitrarily choose to subtract the mean TOF offset following the update given by (5). Therefore, the final mean TOF offset is as close to zero as possible.

3. Results

3.1 Simulation

We used both simulated and clinical data to evaluate the algorithm. First, we used a simulated trues-only 240 million event list of a 27 cm diameter uniform cylinder with 600 ps FWHM TOF resolution. We then degraded the data by biasing the TOF values in the list using an artificial pattern that is representative of the biases caused by the distance of crystals to nearby PMTs as shown in figure 8. This can be compared to the pattern observed for the Gemini TF scanner in figure 2.

We reconstructed subsets of the data using non-TOF reconstruction, and attempted to recover the known TOF offsets using our algorithm. Using a 30 million event portion of the list, a number representative of a single frame of clinical data, we recovered the offsets for 55% of the crystals exactly and 43% were recovered with a 1-bin (25 ps) error. The remaining 2% had errors of 2 bins or more. Using all 240 million events, we recovered 96% exactly as shown in figure 9.

This suggests that a single full-body patient study is likely to contain enough counts to optimally calibrate the scanner, since we can combine the data from all bed positions.

To further test robustness, we included simulated scatter in the data, with a scatter fraction of about 25%. Using 30 million total counts, we still recovered 54% of the TOF offsets exactly. Using 240 million total counts, 95% were recovered exactly as shown in figure 10.

As stated previously, we assume that the average TOF bias of any large region of crystals is zero. We've seen situations, due to the module-based architecture of our scanners, which violate this assumption. To test convergence of the algorithm under these conditions, we added additional bias on a per-module basis as shown in figure 11.

Using 30 million total counts, we still recovered 50% of the offsets exactly. Using 240 million total counts, 94% were recovered exactly as shown in figure 12.

3.2 Philips Healthcare Gemini TF

Next, we evaluated the technique using patient data from commercial and prototype whole body scanners. Unlike the case of simulated data, we do not know the optimal solution, but we can compare our solution to existing calibration results and measure TOF resolution using both algorithms.

First, we randomly selected two clinical whole-body patient studies collected on the same day using our Gemini TF scanner. Data from the first study consisted of 452 million total (prompt + delay) events, or 188 million trues + scatter, collected using 11 bed positions. Data from the second study consisted of 395 million total events, or 164 million trues + scatter, collected using 10 bed positions. We ran our algorithm first using a single central frame of data, and again after combining data from all frames.

Next, we used diagnostic ^{22}Na point source data to measure TOF resolution using the various offset calibration tables. We combined the data from several consecutive days surrounding our patient scan date to improve the statistics in histograms for crystals near the ends of the scanner. Since our daily quality control includes module timing calibration the drift in the TOF bias over this period of time is relatively small.

For each set of point source data, we analyzed the list events to determine the precise location of the point source. Next, for each event in the list, we corrected the TOF value using the TOF offset calibration table under evaluation, and subtracted the expected TOF difference for the LOR. We incremented the resulting TOF error in the two histograms corresponding to the event's crystal endpoints. Finally, we performed a least squares fit of each TOF error histogram with a Gaussian, and computed its FWHM. Histograms of the TOF resolution for all crystals are shown in figure 13.

With no offset calibration, we measured an average FWHM of 699 ps. Using the Philips calibration table updated the morning of the patient studies, we measured 672 ps. Using the calibration table generated by our algorithm and the 11-frame study, we measured 676 ps and 671 ps when using 1 and 11 frames of data, respectively. Using the 10-frame study, we measured 675 ps and 671 ps using 1 and 10 frames of data, respectively.

Although we were able to match the performance the Philips TOF offset calibration, in all cases the TOF resolution is only ~30 ps better than the uncalibrated system. Since Philips performs a preliminary TOF calibration on modules and individual PMT channels, the incremental benefit from any crystal TOF offset calibration is likely to be modest.

3.3 Prototype $LaBr_3$ scanner

In our prototype scanner, TOF calibration consists solely of the crystal TOF offset calibration. No preliminary TOF calibration is perform on modules and individual PMT channels. For this scanner, our standard TOF offset calibration method utilizes a rotating line source.

For this evaluation, we used 153 million total events, or 69 million trues + scatter, from a 4-frame upper body patient scan and the rotating line data collected the same day. We do not have point source data from the same time period, so we used the rotating line data itself to provide a measure of TOF resolution for each crystal.

Using the rotating line data this time, for each crystal in the scanner, we created a histogram of TOF errors, fit it with a Gaussian, and computed its FWHM. Crystal histograms of the results are shown in figure 14.

With no TOF offset calibration, we measured a mean FWHM of 654 ps. Using the rotating line calibration table, we measured 376 ps. Using the patient study, we measured 385 ps and 383 ps when using 1 and 4 frames respectively.

For this scanner, both calibration techniques provide a significant improvement over the uncalibrated system since the TOF offset calibration includes the timing alignment of the modules and PMT channels. We did not achieve the same resolution as the line source method. However, the difference is small, and we only were able to use 4 frames of data.

4. Discussion

Using simulated data with a known timing resolution, we were able to recover TOF offsets with 96% accuracy. Using data from commercial and prototype scanners, where we do not know the true TOF bias, we were able to match the measured TOF resolution of alternative algorithms, which used specialized data acquisitions. However, several assumptions have been made in the algorithm that could affects its robustness as it is applied to new situations. In this section, we will address these assumptions.

At the University of Pennsylvania, our TOF PET calibration and reconstruction processes assume a single TOF resolution for the entire scanner, selected based on the singles count rate during the acquisition. This resolution represents the mean TOF resolution measured during prior point source acquisitions at multiple count rates. During TOF offset calibration, using a single resolution enables us to simplify and accelerate the algorithm by performing the convolution *after* accumulating the ray-traced histograms. If one had per-LOR TOF resolution information, the convolution would be applied after tracing each LOR. Alternatively, it is possible to generalize the algorithm to estimate both the offset *and* resolution required to optimally fit the model histograms to the list histograms. However, based on the TOF resolution variation seen in figures 13 and 14, we did examine the performance impact of a +/−100 ps error in TOF resolution for the simulated data. We found that the degradation of the TOF offset recovery accuracy was well under 1% from the values reported in figure 9.

A second major assumption is that, since the average TOF bias for entire scanner is zero, the average for any large contiguous region of crystals is near zero. This allowed us to neglect the last sum in (3). To understand what happens when this assumption is not true, consider a pair of opposing crystals A and B. When estimating the TOF biases of crystals near A, if the neighborhood of B has a non-zero average TOF bias, an error will be introduced into our estimates of bias near A. When subsequently estimating the biases near B, the errors in the biases near A will affect our estimates near B in the same direction. These errors are not

observable using TOF *differences* measured between these crystals, making the algorithm insensitive to the problem. We have observed at least two situations where this may occur.

The first situation, which applies to both our commercial and prototype scanners, arises because crystals are assembled into modules, which share some electronics processing. A module-wide TOF bias would result in a large region of crystals with non-zero mean. We observed this behavior in our prototype scanner, for which we did not perform a preliminary module timing alignment. We also simulated this phenomenon in our results above. In the early development of our algorithm, this caused the iterative solution to oscillate about the solution. As previously mentioned, introducing relaxation into the iterative update of the TOF offsets as in (5) mitigates this problem. We would not expect to observe this in commercial systems, for which a module timing alignment is performed to optimize the coincidence detection window. In some TOF PET systems, including our Philips Healthcare Gemini TF, additional timing alignment of the PMT channels further reduces the problem.

A second situation can arise because uncertainty in the bias average is related to the size of the object cross-section within a frame of data. Since we only consider LORs that pass through the object, if the object is small – like the frame within a whole-body scan containing the head, then the cumulative TOF error histogram for each crystal will be based on a relatively small region of opposing crystals. This increases the chance that the average TOF bias will be non-zero. During reconstruction, the error also may affect LORs that do not pass close to the region of the object used for calibration. Once again, relaxation mitigates the problem. Another simple solution is to prefer images with a large transverse extent.

A third assumption of our work is that the algorithm can be run during the normal course of clinical operations to provide continuous TOF offset updates for ongoing reconstructions. All phases of the algorithm are easily parallelizable. Execution time on a single 39 million event frame of Gemini TF patient data for a multi-threaded version on a dual-CPU 2.8 GHz Intel Xeon X5660 machine includes 30.9 seconds to ray-trace an existing non-TOF image and 47.5 seconds to histogram existing TOF single scatter simulation data. The last phase, which includes histogramming the list data and updating the TOF offsets using maximum cross-correlation, is currently single-threaded and takes 23.4 seconds per iteration. A complete single-frame, 10-iteration run takes a total of 5 minutes and 25 seconds. A 10-frame run would take just under one hour. This time could be reduced significantly by parallelizing the histogramming phase and/or distributing the algorithm across multiple machines. The algorithm also would map well to a GPU-based implementation.

5. Conclusion

In this paper we have presented a novel algorithm for TOF offset calibration from clinical, rather than specialized, data sets. We have verified that the algorithm accurately recovers known TOF offsets using simulated data. We also confirmed that, for TOF PET scanners at the University of Pennsylvania, the algorithm performs as well as existing calibration techniques using the quantity of data typically collected during a single patient study. Using data from multiple patients, even higher calibration stability and precision could be achieved. By using available computational resources, it should be possible to maintain a continuously refined TOF calibration with no user intervention. Since we generate the calibration from the data itself, we no longer need to archive timing calibration files corresponding to the patient data, or be concerned that calibration files for archived studies are missing or suboptimal. The algorithm can be applied to any current or historical data set in order to ensure the maximum benefit from TOF PET reconstruction.

Acknowledgments

This work was supported by the National Institutes of Health under grant R01 CA113941.

References

Bettinardi V, Presotto L, Rapisarda E, Picchio M, Gianolli L, Gilardi MC. Physical performance of the new hybrid PET/CT Discovery-690. Med Phys. 2011; 38(10):5394–5411. [PubMed: 21992359]

Casey, ME.; Chen, M.; Gremillion, TG.; Hayden, CH.; Lenox, MW.; Panin, VY. Systems and methods for calibrating time alignment for a positron emission tomography (PET) system. US Patent. 8089043B2. 2012.

Daube-Witherspoon ME, Surti S, Perkins A, Kyba CC, Wiener R, Werner ME, Kulp R, Karp JS. The imaging performance of a $LaBr_3$-based PET scanner. Phys Med Biol. 2010; 55(1):45–64. [PubMed: 19949259]

El Fakhri G, Surti S, Trott CM, Scheuermann J, Karp JS. Improvement in lesion detection with whole-body oncologic time-of-flight PET. J Nucl Med. 2011; 52(3):347–353. [PubMed: 21321265]

Griesmer, JJ.; Laurence, LT. Calibrating the coincidence timing utilized in time-of-flight measurements in positron emission tomography. US Patent. 7414246. 2008.

Jakoby BW, Bercier Y, Conti M, Casey ME, Bendriem B, Townsend DW. Physical and clinical performance on the mCT time-of-flight PET/CT scanner. Phys Med Biol. 2011; 56(8):2375–2389. [PubMed: 21427485]

Kadrmas DJ, Casey ME, Conti M, Jakoby BW, Lois C, Townsend DW. Impact of time-of-flight on PET tumor detection. J Nucl Med. 2009; 50(8):1315–1323. [PubMed: 19617317]

Karp JS, Kuhn A, Perkins AE, Surti S, Werner ME, Daube-Witherspoon ME, Popescu L, Vandenberghe S, Muehllehner G. Characterization of a time-of-flight PET scanner based on lanthanum bromide. Proc IEEE Nucl Sci Symp. 2005; 4:1919–1923.

Karp JS, Surti S, Daube-Witherspoon ME, Muehllehner G. Benefit of time-of-flight in PET: experimental and clinical results. J Nucl Med. 2008; 49(3):462–470. [PubMed: 18287269]

Lenox MW, Atkins BE, Pressley DR, McFarland A, Newport DF, Siegel SB. Digital time alignment of high resolution PET Inveon block detectors. IEEE Nucl Sci Symp Conf Record. 2006:2450–2453.

Lenox MW, Burbar Z, Young J, Gremillion T, Knoess C. Coincidence time alignment of high resolution planar detectors. Proc IEEE Nucl Sci Symp. 2002; 2:956–959.

Lois C, Jakoby BW, Long MJ, Hubner KF, Barker DW, Casey ME, Conti M, Panin VY, Kadrmas DJ, Townsend DW. An assessment of the impact of incorporating time-of-flight information into clinical PET/CT imaging. J Nucl Med. 2010; 51(2):237–245. [PubMed: 20080882]

Perkins AE, Werner M, Kuhn A, Surti S, Muehllehner G, Karp JS. Time-of-flight coincidence timing calibration techniques using radioactive sources. Proc IEEE Nucl Sci Symp. 2005; 5:2488–2491.

Surti S, Kuhn A, Werner ME, Perkins AE, Kolthammer J, Karp JS. Performance of Philips Gemini TF PET/CT scanner with special consideration for its time-of-flight imaging capabilities. J Nucl Med. 2007; 48(3):471–480. [PubMed: 17332626]

Surti S, Scheuermann J, El Fakhri G, Daube-Witherspoon ME, Lim R, Abi-Hatem N, Moussallem E, Benard F, Mankoff D, Karp JS. Impact of time-of-flight on whole-body oncology studies: a human observer lesion detection and localization study. J Nucl Med. 2011; 52(5):712–719. [PubMed: 21498523]

Thompson CJ, Camborde M, Casey ME. A central positron source to perform the timing alignment of detectors in a PET scanner. IEEE Trans Nucl Sci. 2005; 52(5):1300–1304.

Werner ME, Surti S, Karp JS. Implementation and evaluation of a 3D PET single scatter simulation with TOF modeling. Proc IEEE Nucl Sci Symp. 2006; 3:1768–1773.

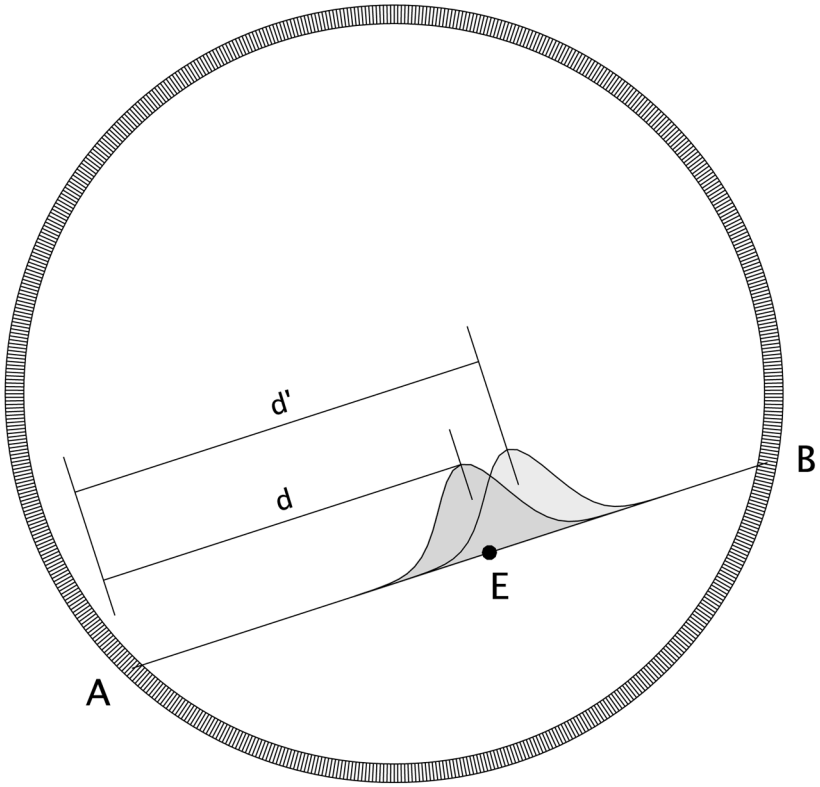

Figure 1.
TOF resolution model for an emission from point *E* with and without TOF bias

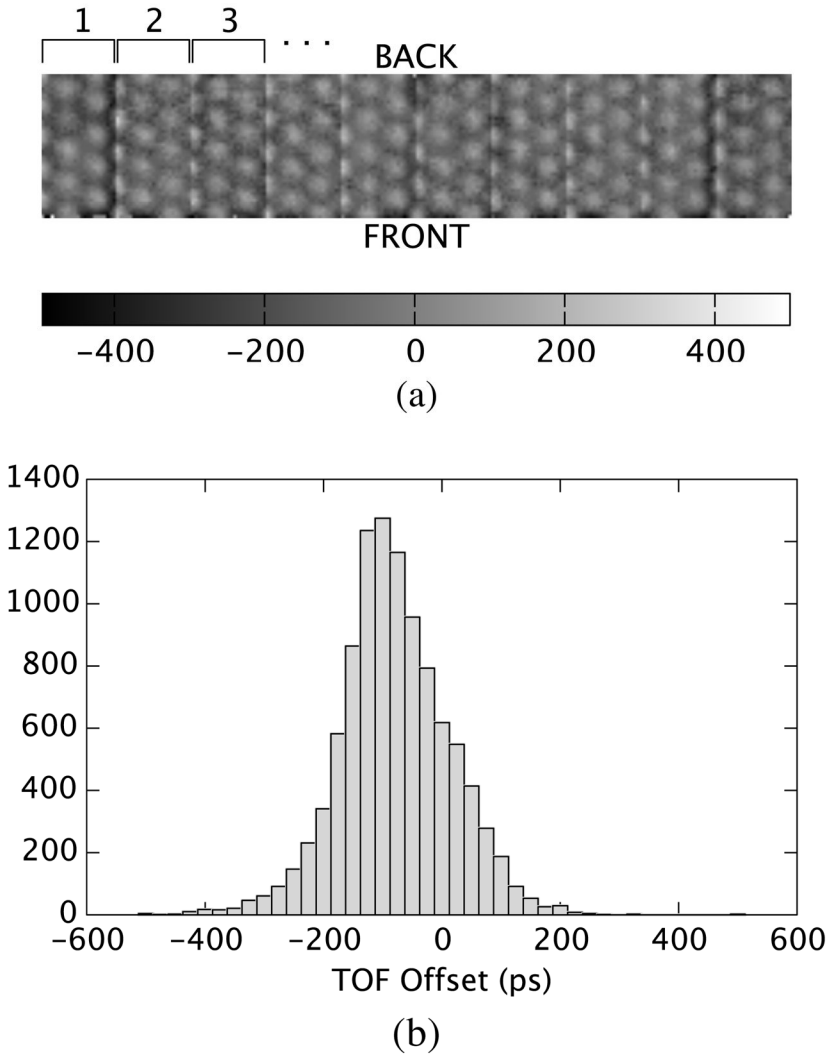

Figure 2.
TOF offsets obtained from Philips software for the first 10 modules of our Gemini TF scanner as (a) an X–Z crystal map and (b) a histogram.

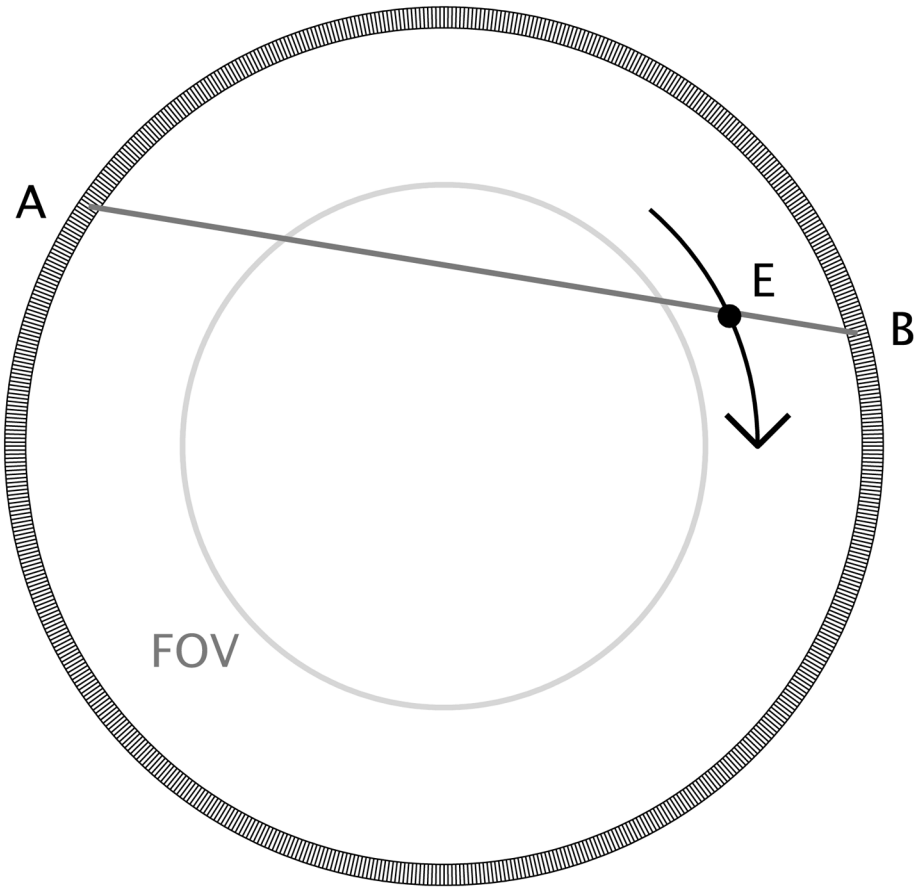

Figure 3.
Transverse view of a rotating line source. An emission from the line source at *E* is detected by crystals *A* and *B*.

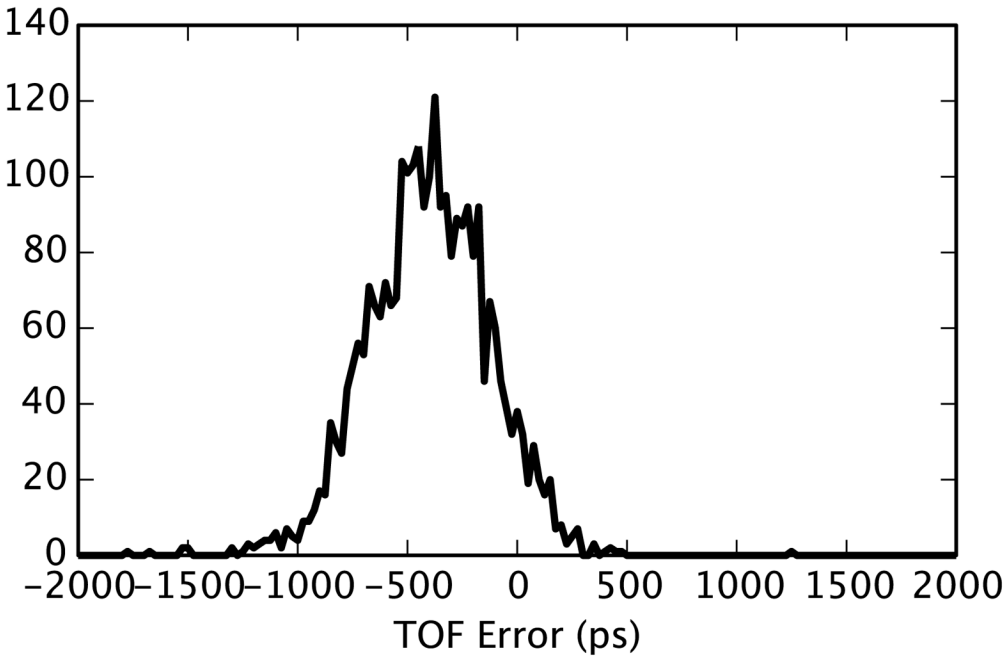

Figure 4.
Histogram of TOF errors for all events from rotating line source having a selected crystal as one endpoint. The crystal exhibits a negative TOF bias.

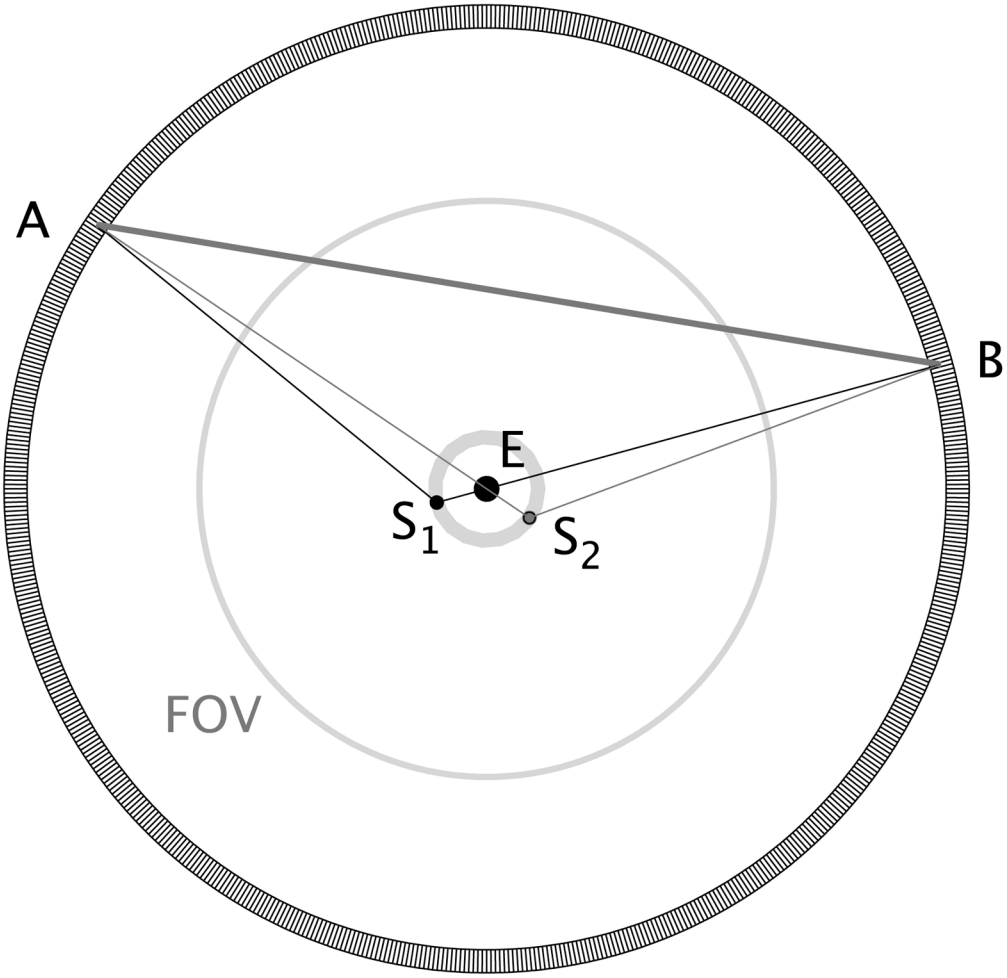

Figure 5.
An emission from point *E* is detected at points *A* and *B* after scattering at S_1 or S_2.

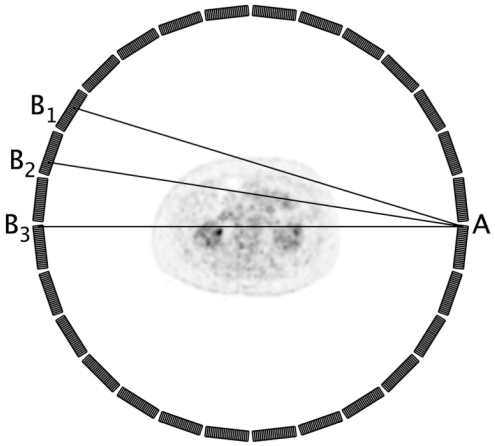

(a)

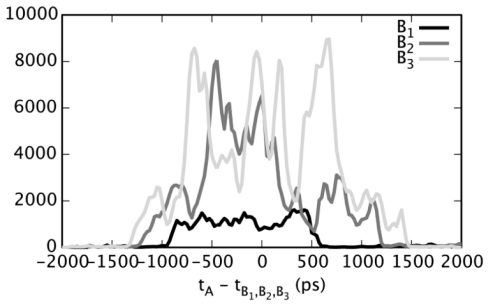

(b)

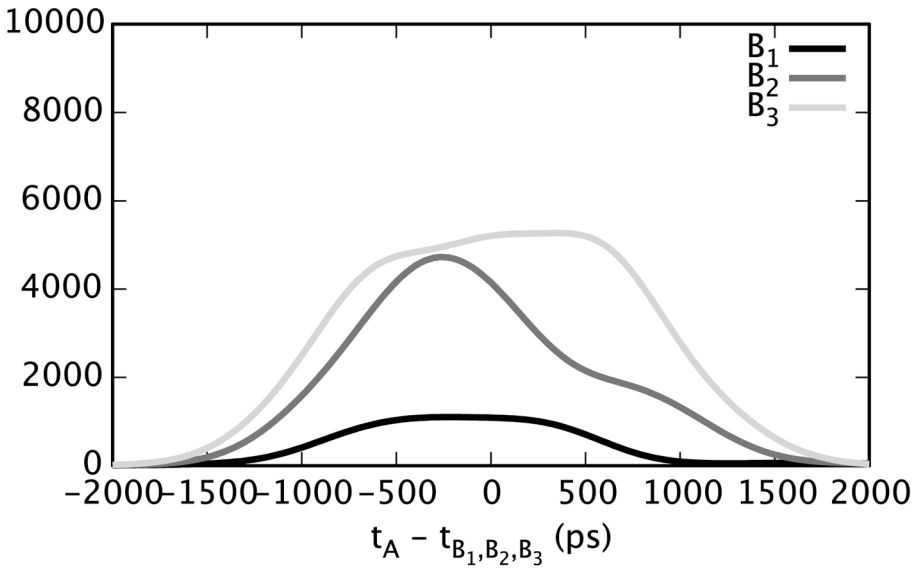

(c)

Figure 6.

(a) Traces through the patient image in result in (b) raw TOF profiles for crystal A representing the image intensity vs. $t_A - t_B$. These profiles are convolved with the estimated TOF resolution in (c).

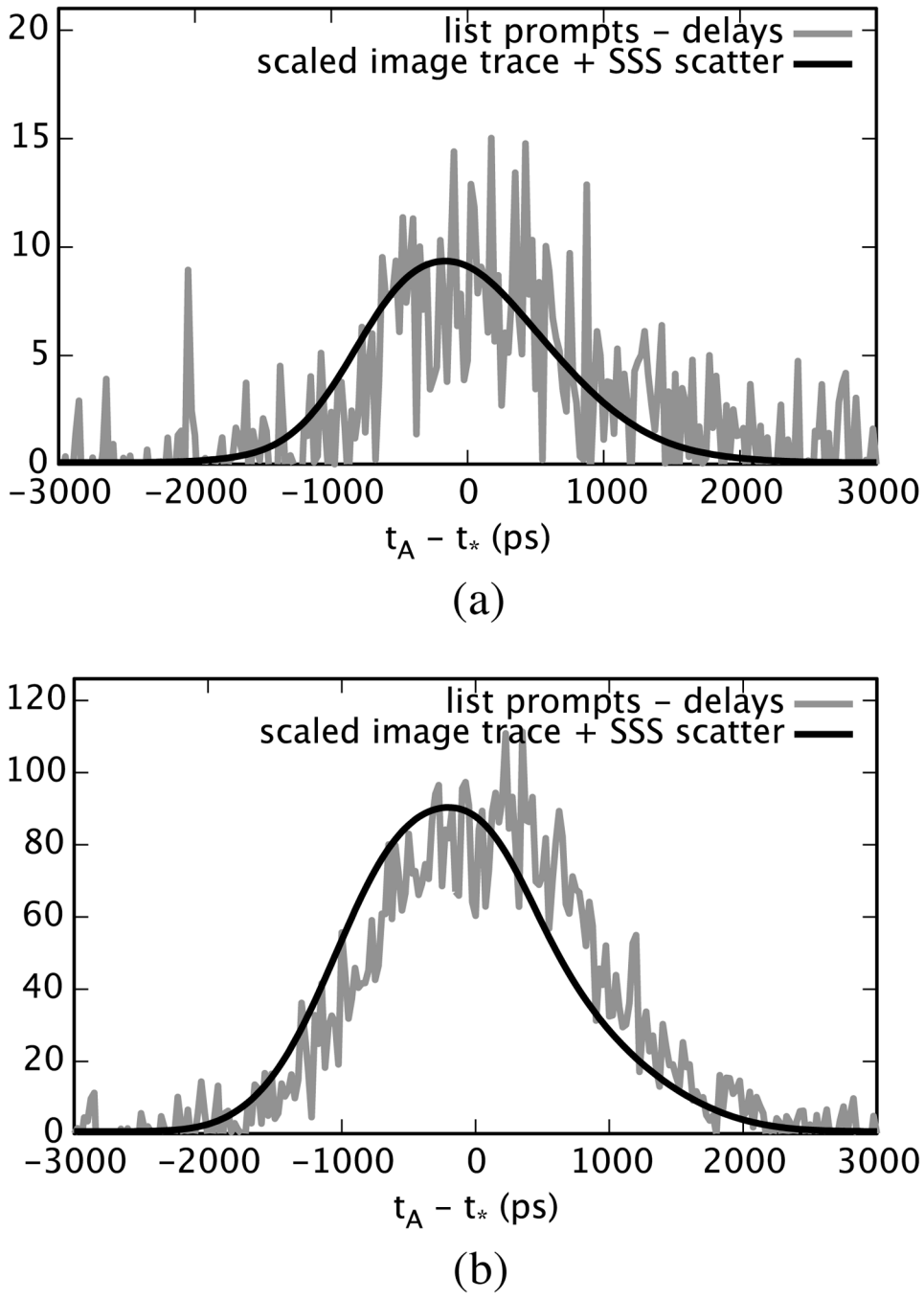

Figure 7.
For a single crystal, the list TOF histogram vs. the model TOF histogram using (a) 1 bed position and (b) all 11 bed positions of a typical patient study.

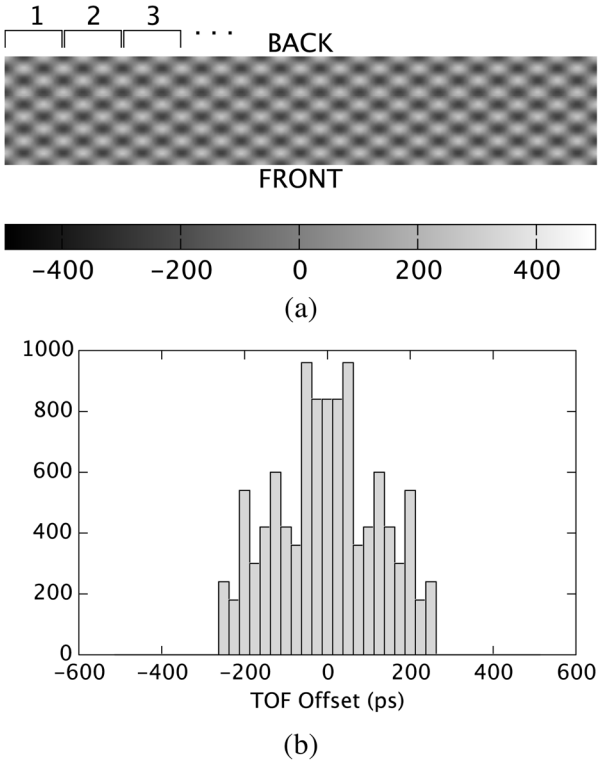

Figure 8.
TOF offsets for the first 10 modules of our simulated scanner as (a) an X–Z crystal map and (b) a histogram.

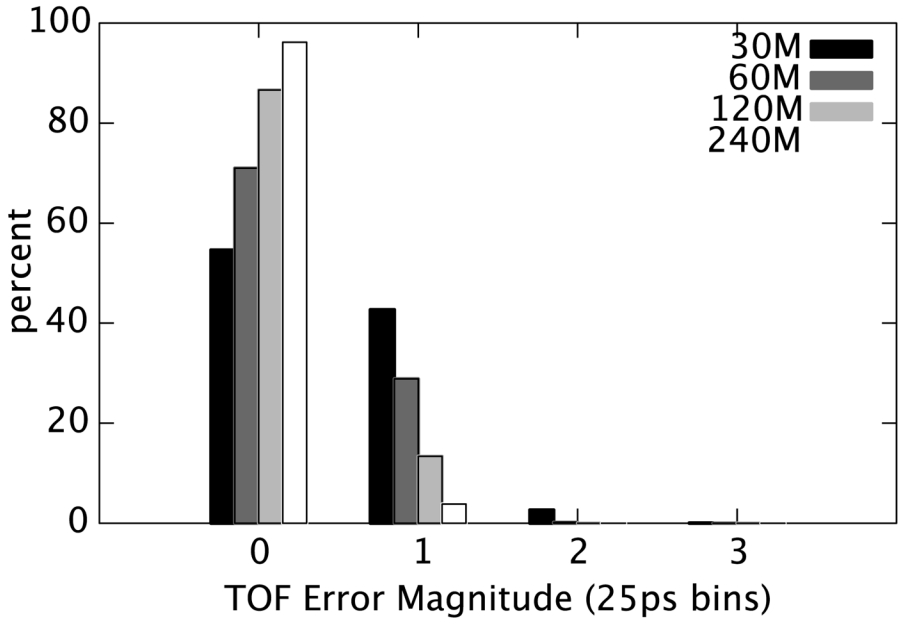

Figure 9.
Percentage of recovered TOF offsets with errors of 0–3 bins.

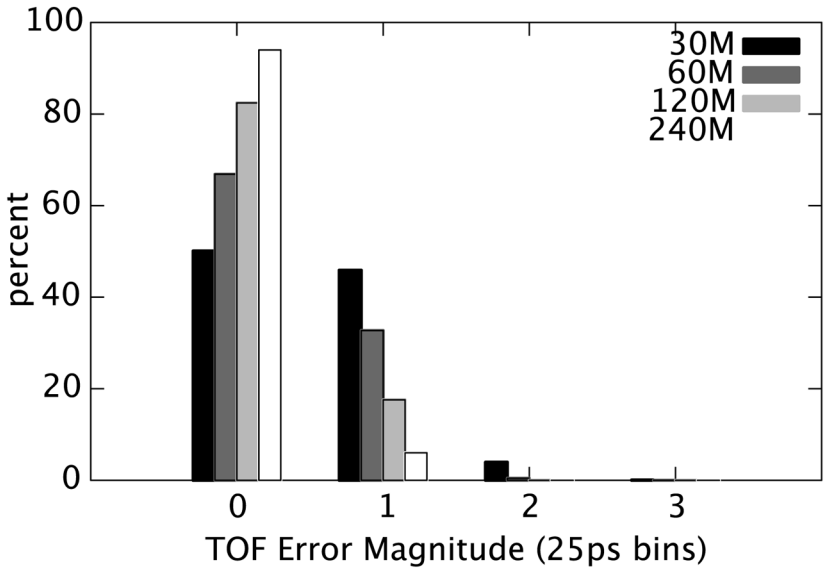

Figure 10.
Percent recovery with scatter.

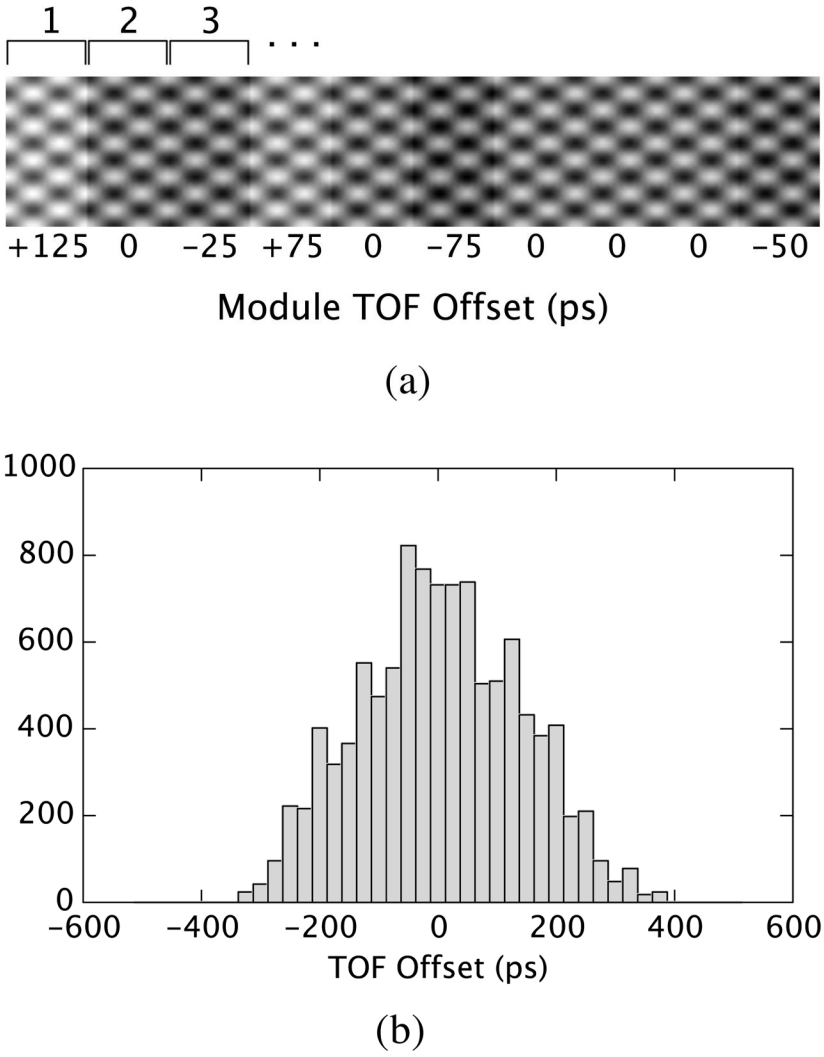

Figure 11.
TOF offsets for the first 10 modules of a simulated scanner incorporating random per-module biases as (a) an X-Z crystal map and (b) a histogram.

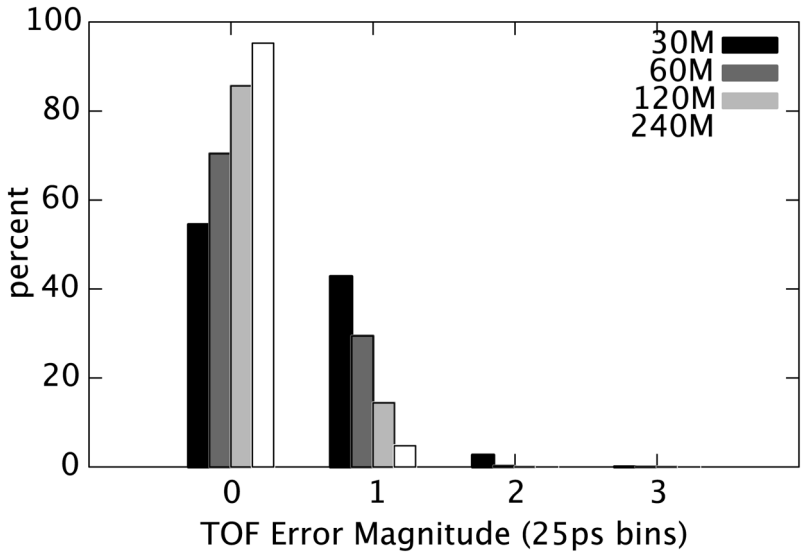

Figure 12.
Percent recovery with additional per-module bias.

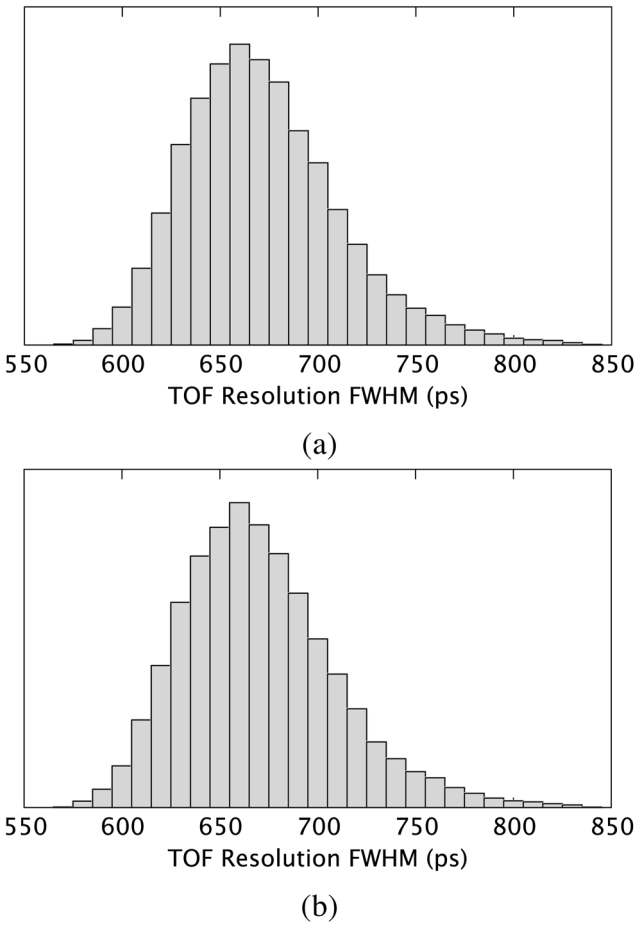

Figure 13.
Histogram of TOF resolution of all crystals in Gemini TF for a point source using the TOF offsets obtained from (a) Philips software and (b) our algorithm applied to an 11-frame patient study.

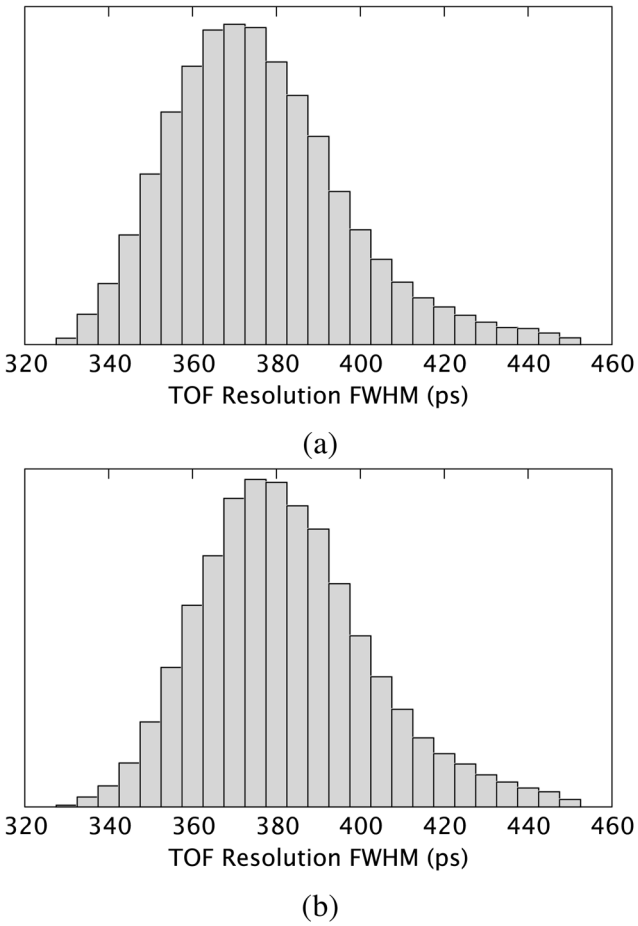

Figure 14.
Histogram of TOF resolution of all crystals in our prototype scanner for a point source using TOF offsets obtained from (a) a rotating line and (b) our algorithm applied to a 4-frame patient study.